Quarterly Journal of the Royal Meteorological Society   *Q. J. R. Meteorol. Soc.* 136: 1773–1787, October 2010 Part A

Forced gravity wave response near the jet exit region in a linear model

Shuguang Wang,[a] Fuqing Zhang[b]* and Craig C. Epifanio[a]

[a]*Department of Atmospheric Sciences, Texas A&M University, College Station, Texas, USA*

[b]*Department of Meteorology, Pennsylvania State University, University Park, Pennsylvania, USA*

*Correspondence to: Fuqing Zhang, Department of Meteorology, Pennsylvania State University, University Park, PA 16802, USA. E-mail: fzhang@psu.edu

This study investigates the propagation of gravity waves in the region of significant horizontal and vertical shear associated with a localized atmospheric jet using a linear model. Gravity waves are produced in the linear model by imposing prescribed divergence/convergence forcing of various scales near the core of an idealized local jet. The spatial structures of these forced gravity waves are nearly steady after a few inertial periods, despite the amplitudes slowly increasing with time.

Linear model simulated wave response to prescribed forcing shows limited dependence on the scales of the forcing. It is found that the wave structure (e.g. horizontal/vertical wavelengths, phases and locations) away from the forcing are largely constrained by the environmental wind shear through the wave capture mechanism. Consequently, simulated gravity wave activities have the tendency to be focused on the vicinity where the line of constant shear aspect ratio approximates to the characteristic large-scale environmental aspect ratio (f/N). Ray tracing analysis is further used to demonstrate that wave capturing is the consequence of different influences of the horizontal and vertical shears upon longer and shorter waves. Copyright © 2010 Royal Meteorological Society

Key Words: inertia–gravity waves; wave capture; linear wave solution; vortex dipoles

Received 8 March 2009; Revised 17 April 2010; Accepted 13 June 2010; Published online in Wiley Online Library 12 October 2010

Citation: Wang S, Zhang F, Epifanio CC. 2010. Forced gravity wave response near the jet exit region in a linear model. *Q. J. R. Meteorol. Soc.* **136**: 1773–1787. DOI:10.1002/qj.676

1. Introduction

Atmospheric jets are known to be responsible for generating low-frequency inertia–gravity waves with characteristic horizontal wavelengths of several hundred kilometres, as suggested by many studies based on observations (e.g. Uccellini and Koch, 1987; Sato, 1994; Plougonven and Teitelbaum, 2003; Wu and Zhang, 2004). Numerical studies based on simulations of idealized jets during life cycles of baroclinic waves (O'Sullivan and Dunkerton, 1995; Zhang, 2004; Wang and Zhang, 2007) and of localized jets associated with vortex dipoles (Viudez, 2007; Snyder *et al.*, 2007, 2009; Wang *et al.*, 2009) provide further evidence of wave generation from jets.

While various efforts focus on explaining the source and forcing mechanisms of these gravity waves (Plougonven and Zhang, 2007, hereafter PZ07; Snyder *et al.*, 2009; Wang and Zhang, 2010), recent studies also suggest the propagation effect in the region of strong shear may also be as important as the generation mechanisms to the extent that wave characteristics may be largely determined/selected by the environmental shear (Plougonven and Snyder, 2005; Lin and Zhang, 2008). Bühler and McIntyre (2005) and an earlier study by Badulin and Shrira (1993) suggested that the wave-capture mechanism is important for wave propagation in constraining wave characteristics in an environment of strong horizontal and vertical wind variations. Through the use of a ray-tracing model, Lin and Zhang (2008) demonstrated that wave characteristics may change significantly along the propagation path in the baroclinic jet–front system.

In the meantime, even if the forcing of the waves is known, interpretation of wave response in a nonlinear dynamic problem is often complicated. The standard way to overcome the difficulty is to treat the wave response as a linear disturbance about a balanced background state, which may allow the wave response to be cleanly separated from the forcing, and also allow the structure and propagation of the waves to be interpreted using the linear theory (e.g. Fritts and Alexander, 2003).

The current study develops a non-hydrostatic numerical model linearizable about any arbitrary background state, along with a ray-tracing technique, to examine (1) the propagation effect on the waves in the complex environment of the jet, and (2) the relationship between the wave structure and the spatial scales of the forcing.

This article will be structured as follows. The linear model and the ray tracing method are introduced in section 2. Forced linear wave response to prescribed forcing at different scales in mid-tropospheric dipoles is explored in section 3. Ray tracing analysis is discussed in section 4. Wave response to forcings in a surface-based dipole is discussed in section 5. Concluding remarks are in section 6.

2. A linear model and ray tracing model

2.1. Basic formulation of a linear model

The model is formulated in the non-hydrostatic, compressible Boussinesq framework and uses vorticity and divergence as prognostic variables following PZ07. We first separate the wind components (u,v,w), potential temperature θ, and Boussinesq disturbance pressure p into large-scale background and disturbance, i.e. $u = u_B + u'$, $v = v_B + v'$, $w = w_B + w'$, $\theta = \theta_B + \theta'$, $p = p_B + p'$, and $\vec{U_B} = (u_B, v_B, w_B)$, $\vec{u} = (u', v', w')$. Letting the disturbance relative vorticity and horizontal divergence be denoted by ς' and δ', the linearized equation set in the compressible non-hydrostatic flow is written as, with the primes dropped:

$$\frac{\partial \delta}{\partial t} + \vec{U_B} \cdot \nabla \delta + \left[\left(\frac{\partial}{\partial x} \vec{U_B} \right) \cdot \nabla u + \left(\frac{\partial}{\partial y} \vec{U_B} \right) \cdot \nabla v \right] + \left\{ \nabla_H \left(\vec{u} \nabla \vec{U_B} \right) \right\} - f\varsigma + \Delta p = F_\delta \tag{1.1}$$

$$\frac{\partial \varsigma}{\partial t} + \vec{U_B} \cdot \nabla \varsigma + \left[- \left(\frac{\partial}{\partial y} \vec{U_B} \right) \nabla u + \left(\frac{\partial}{\partial x} \vec{U_B} \right) \nabla v \right] + \left\{ \vec{k} \cdot \nabla \times \left(\vec{u} \nabla \vec{U_B} \right) \right\} + f\delta = F_\varsigma \tag{1.2}$$

$$\frac{\partial \theta}{\partial t} + \vec{U_B} \cdot \nabla \theta + \left\{ u \frac{\partial \theta_B}{\partial x} + v \frac{\partial \theta_B}{\partial y} \right\} + w \frac{\partial \theta_B}{\partial z} = F_\theta \tag{1.3}$$

$$\frac{\partial w}{\partial t} + \vec{U_B} \cdot \nabla w + \left\{ \vec{U} \cdot \nabla w_B \right\} = -p_z + \frac{g}{\Theta_r} \theta \tag{1.4}$$

$$\frac{\partial p}{\partial t} = -{C_s}^2 \cdot \left(\delta + \frac{\partial w}{\partial z} \right) \tag{1.5}$$

where C_s is the speed of sound (300 m s^{-1}), Θ_r is a constant reference value (300 K), F_δ, F_ς and F_θ are the forcing terms that are functions of the background states. The terms in the curly and square brackets in Eqs (1.1)–(1.5) denote the shear terms. The advection and shear terms in Eq. (1.5) are neglected following the argument in Epifanio and Rotunno (2005) (refer to PZ07 for details on the derivation and scale analysis of the equation set (1.1)–(1.5)).

The linear model equation set (1.1)–(1.5) has five prognostic variables: horizontal divergence, relative vorticity, vertical velocity, potential temperature and Boussinesq disturbance pressure. Equations (1.1)–(1.5) are closed by computing the perturbation winds, which are diagnosed via the two-dimensional (2D) Helmholtz decomposition $\mathbf{u} = \nabla\phi - \mathbf{k} \times \nabla\psi$, where the potential ϕ and stream function ψ are related to the divergence and vorticity by

$$\delta = \nabla_H^2 \phi, \zeta = \nabla_H^2 \psi. \tag{2}$$

Periodic boundary conditions are adopted for ϕ and ψ for convenience, since the disturbance of interest does not reach the lateral boundaries.

The terms in the curly brackets in Eqs (1.1)–(1.5) denote the shear terms associated with the horizontal and vertical wind shears (shear terms A), while the square brackets denote the additional terms (shear terms B) in the u–v-based linear model.

2.2. Numerics of the linear model

Numeric details are given below. All variables are staggered on half levels vertically with the vertical velocity on full levels. The 'A grid' staggering is used for all the prognostic variables in the horizontal, including δ and ζ. Advection terms are fourth-order accurate in the inner domain and second-order accurate near the boundaries. The model uses the split-explicit operator splitting described in Skamarock and Klemp (1992) and Durran (1999, section 7.3.2). The 3rd-order Runge–Kutta scheme of Wicker and Skamarock (2002) is used for the large time step, while the small time step is forward–backward. Rigid top and bottom boundary conditions and simple outflow lateral boundary conditions are applied to the rectangular domain. In addition, Rayleigh damping is adopted to minimize possible wave reflections near all the boundaries. The fast Poisson solver in the 'Fishpack' package is used to obtain horizontal winds from the divergence and vorticity (Swarztrauber and Sweet, 1975).

Some simple tests (e.g. the test of the channel hydrostatic wave in Skamarock and Klemp (1994)) have been performed to validate the above time-matching scheme. The divergence–vorticity-based model can be easily converted and gives nearly identical solution to a u–v-based model without much modification to the code. Nevertheless, the current model has the advantage of directly applying the divergence and vorticity forcing.

In all the linear model runs discussed in this study, the horizontal (vertical) grid spacing is 30 km (200 m) for a rectangular domain (142 × 151 × 120). The maximum Rayleigh damping coefficient is 10^{-5} s^{-1}. The 4th-order horizontal filter has a coefficient of $10^{-2}(\Delta x)^4/\Delta t$.

2.3. Ray tracing model

To understand characteristics of the waves as simulated by the linear model, a ray tracing code (GROGRAT: Marks and Eckermann, 1995) is further adopted. This code is modified for calculation in the f plane and for regional-scale applications as in Lin and Zhang (2008) and Wang *et al.* (2009). The ray tracing is based on the dispersion relation for plane waves:

$$\omega_{\mathrm{i}}^2 = (\omega - u_{\mathrm{B}}k - v_{\mathrm{B}}l - w_{\mathrm{B}}m)^2 = \frac{N^2(k^2+l^2)+f^2(m^2)}{k^2+l^2+m^2}, \quad (3)$$

where ω_{i} and ω are intrinsic frequency and absolute frequency, (k, l, m) are three components of the wave-number vector, and u_{B}, v_{B}, w_{B} are the components of the spatially and temporally varying background winds.

Note that this ray tracing model is based on the standard asymptotic Wentzel–Kramers–Brillouin (WKB) assumption, which is close to the linear model solution without the terms in the curly and square brackets in Eqs (1.1)–(1.5) that are associated with the horizontal and vertical wind shears.

3. Wave response to the prescribed forcing in a QG dipole

3.1. Dipole jet, forcing and wave response

First, a kinematically consistent jet flow is created by adding a prescribed quasi-geostrophic (QG) potential vorticity (QGPV) anomaly to an undisturbed reference state on an f plane. The reference flow is assumed to have uniform static stability and constant zonal wind U, while the QGPV anomaly is described by

$$Q' = \pm 1.75 \times 10^{-4} \cdot \left\{\cos^2(r_{10}\cdot \pi/2) - \cos^2(r_{20}\cdot\pi/2)\right\}, \quad (4)$$

where

$$r_{10} = \begin{cases} r_1, \text{if } r_1 \le 10, \\ r_1 = \sqrt{(x-x_1)^2 + (y-y_1)^2 + \gamma\cdot(z-z_0)^2}\Big/R_0, \end{cases}$$

$$r_{20} = \begin{cases} r_2, \textit{if } r_2 \le 10, \\ r_2 = \sqrt{(x-x_2)^2 + (y-y_2)^2 + \gamma\cdot(z-z_0)^2}\Big/R_0. \end{cases}$$

Unless otherwise stated, the parameters for the reference state are the squared buoyancy frequency $N^2 = 2\times 10^{-4}\ \mathrm{s}^{-2}$, $U = -5\ \mathrm{m\ s}^{-1}$ and the Coriolis parameter $f = 10^{-4}\ \mathrm{s}^{-1}$. The disturbance QGPV parameters are given by $R_0 = 1800$ km and $\gamma = 9.8$. The positions of the anomalies (*x1, y1, z0*) (*x2, y2, z0*) are indicated in Figure 1. The domain is rectangular with $x = y = 0$ the centre of the domain and $z = 0$ the ground.

Figure 1 shows the structure of the quasi-geostrophically balanced jet with the maximum zonal wind $U_{\mathrm{B}} = \sim 30\ \mathrm{m\ s}^{-1}$. Different from the Ertel PV inversion, the QGPV inversion preserves the symmetry between the cyclone and the anticyclone. Enhanced and reduced buoyancy frequency is also found in the cyclonic and anticyclonic regions near the level of the QGPV maxima at $z = 12$ km. This is consistent with the conceptual picture of the circulation associated with the PV thinking. The forcing is located in the jet core (near the wind speed maximum) and has the Gaussian shape:

$$F_\delta(x,y,z) = \Delta_0 \cdot \exp\left\{-\frac{(x-x_c)^2+(y-y_c)^2}{{R_{\mathrm{H}}}^2} - \frac{(z-z_c)^2}{R_z^2}\right\}, \quad (5)$$

where R_{H} and R_z indicates the horizontal and vertical scales of the forcing. This forcing is symmetric about the jet core. This study is limited to prescribed time-independent forcing in F_δ with the same amplitude $\Delta_0 = 3\times 10^{-10}\ \mathrm{s}^{-2}$ while $F_\varsigma = F_\theta = 0$.

Figures 2(a) and 3(a) show the wave response at 210 h with the Gaussian-shaped forcing that has half-width horizontal (vertical) scale of 225 (1.5) km (hereafter referred to as the control experiment or 'CNTL'). Wave phase is distorted in the region near the wave source such that the wave phase is orientated northwest–southeast. Subsequently, waves propagate toward the exit region of the jet displaying asymmetric patterns between the cyclonic and anticyclonic sides of the dipole jet (Figure 2(a)). As the wave packets propagate further upward and downward, the horizontal wavelength decreases continuously and smoothly toward the smallest resolvable scale of the linear model (Figure 3(a)). Eventually these wave packets will encounter critical levels where the mean wind decreases to the phase speed of the wave packet. The actual wave breaking due to the critical-level effect is nonlinear and small-scale such that it cannot be resolved but is handled by the artificial numerical diffusion implemented in the linear model.

3.2. Effects of background static stability and shear terms

The linear divergence–vorticity-based model documented in the previous section is first used to study the effects of varying background static stability and shear terms on the spatial wave structure, propagation and frequency.

Figures 2(b) and 3(b) show the vertical velocity simulated by the linear model at 210 h in Experiment 'Nconst' in which the background θ_{B} in CNTL is replaced by the mean θ_{B} at each model level (so that the background N is horizontally uniform with the squared buoyancy frequency $N^2 = 2\times 10^{-4}\ \mathrm{s}^{-2}$). There is only a slight change of the wave pattern in Nconst compared to CNTL (Figures 2(b) and 3(b) vs. Figures 2(a) and 3(a)), suggesting the asymmetry in background stratification between the cyclonic and anticyclonic sides of the dipole jet has minimal effects on the propagation, structure and characteristics of the forced linear wave response. Experiment 'NoShearA' is the same as CNTL but removes the shear terms in the curly brackets in Equations (1.1)–(1.5) from the linear model. There is only a slight difference in the amplitude of the wave response but the wave pattern becomes noticeably more symmetric between the cyclonic and anticyclonic sides of the dipole jet (Figure 2(c)) than in the CNTL experiment (Figure 2(a)). The shear terms in the curly brackets of Eqs (1.1)–(1.5) also have minimal impact on the wave response along the vertical cross-section through the centre of the jet (Figure 3(c) vs. Figure 3(a)).

Figures 2(d) and 3(d) shows Experiment 'NoShearB' that is the same as CNTL but removes all shear terms in both the curly and square brackets in Eqs (1.1)–(1.5) from the linear model. Compared with CNTL in Figures 2(a) and 3(a), wave amplitude is reduced by less than 10% in terms of the maximum vertical velocity while the wave pattern becomes nearly symmetric (Figures 2(d) and 3(d)). If static stability is further replaced by the level average value as in 'Nconst', the vertical velocity pattern will become perfectly symmetric (not shown).

In short, the above sensitivity experiments demonstrate that the asymmetries of wave response in the standard

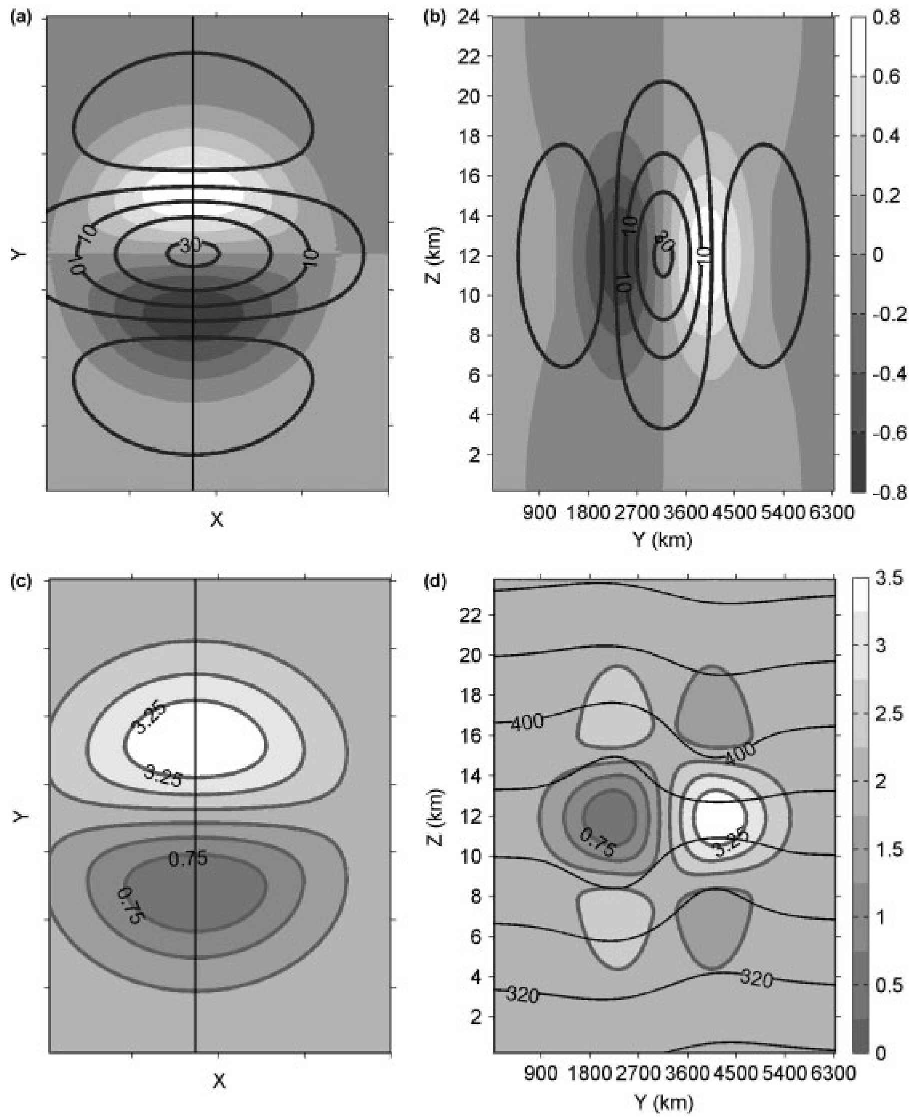

Figure 1. Horizontal wind in the x direction (U_B, solid, every 10 m s^{-1}) and vertical relative vorticity (shading, scaled by $f = 10^{-4}$ s^{-1}) are plotted (a) at the middle level (12 km) and (b) along the vertical cross-section. Squared buoyancy frequency scaled by 10^4 s^{-2} ($N^2 \times 10^4$, every 0.5) is plotted (c) at the middle level and (d) along the vertical cross-section. Isentropes (thick lines, every 20 K) are also shown in (d). The distance between ticks in left panels is 900 km. The straight line in the left panels indicates the vertical cross sections in the corresponding right panels.

(CNTL) dipole–jet background comes mostly from the square bracket terms in the linear model with small contributions from the shear terms in the curly brackets and asymmetries in the background stratification between the cyclonic and anticyclonic sides.

3.3. *The rotational wind response*

In the CNTL experiment described above, the linear response grows with time, although the forcing is time-independent along with the fixed background state. The linear response consists of two parts: gravity waves (the divergence modes) and the balanced rotational winds (the rotational modes). A steady-state solution is not available for CNTL because the shear terms may induce instability. This instability has also been discussed by Snyder *et al.* (2009).

Figure 4 shows the simulated relative vorticity at 2 km above the jet core at 210 h from experiments CNTL, NoShearA and NoShearB, respectively. In CNTL (Figure 4(a)), the constant divergence forcing induces relative vorticity above the forcing and noticeably negative vorticity in both anticyclonic and cyclonic regions. Setting N^2 to be constant at each level in the linear model further enhances the negative vorticity in the anticyclonic region (not shown). On the other hand, Figure 4(a)–(b) show that wind vectors have a strong rotational component in both the cyclonic and anticyclonic sides of the jet, while further neglecting the shear terms in the square brackets (NoShearB) removes nearly all the rotational component in the two sides of the jet except for small areas on the leading edge of the jet.

Figure 5 shows the time series of kinetic energy associated with the non-divergent winds (inverted from the stream function) and irrotational winds (inverted from wind potential). The rotational response dominates over divergent response throughout the model integration and show exponential growth after 200 h. The irrotational winds remain nearly steady for the first 500 hours but obtain a small upward trend near the end of the integration. The time series are not intended to separate the rotational modes and divergent modes, but they are indicative of the rotational nature of the possible instability model. In fact, we have also performed linear model experiments with initially

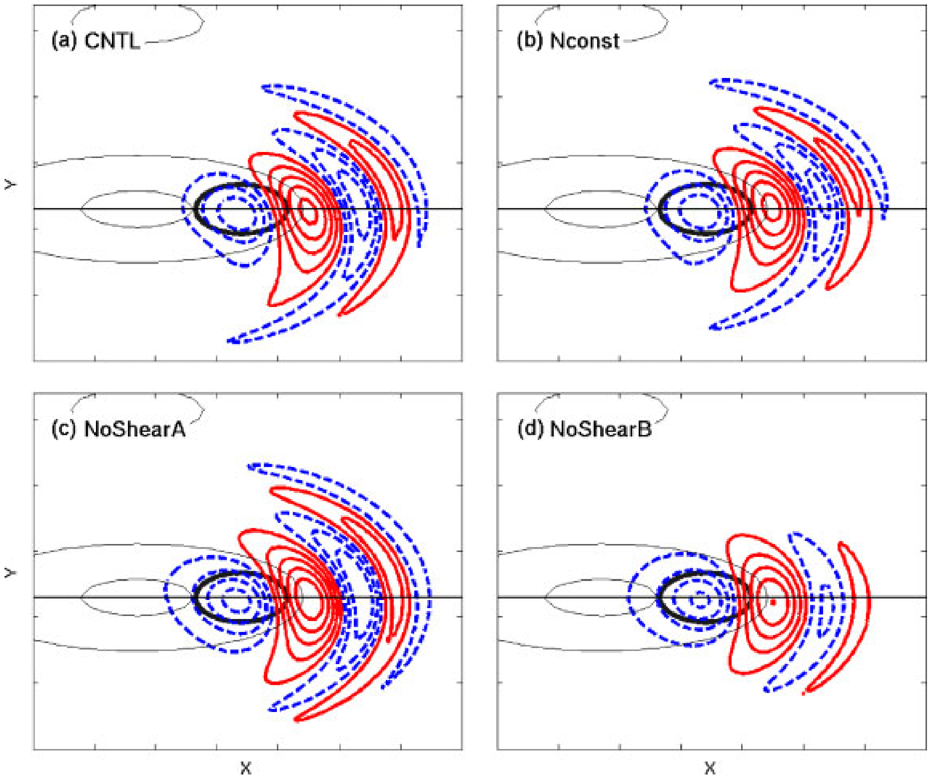

Figure 2. (a) Vertical velocity (contour interval (ci) = 2.5×10^{-4} m s^{-1}, positive, solid; negative, dashed; zero contours omitted) at 14 km at 210 h from CNTL. (b) Same as (a) except that background static stability is constant (Nconst). (c) As (a) but without the shear terms A (NoShearA). (d) As (a) but with all shear terms in both the curly and square brackets in Equations (1.1)–(1.5) excluded (NoshearB). The light contours are wind speed (20, 30 m s^{-1}) of the background wind. The solid straight lines indicate the corresponding vertical cross-sections in Figure 3. The distance between ticks is 300 km. This figure is available in colour online at wileyonlinelibrary.com/journal/qj

random noises but without forcing. Such experiments also produce slowly growing amplitudes of rotational winds, suggesting the existence of the slow instability. Nevertheless, the possible instability is beyond the scope of the current study.

3.4. *Wave response to forcing at different scales*

This section focuses on a set of linear model simulations of gravity waves that are forced by the prescribed forcings with different half horizontal/vertical scales (R_H and R_z in Eq. (5)). We will compare the gravity wave response in these simulations, particularly wave pattern, wave amplitude, wave aspect ratio and wave propagation.

The horizontal and vertical scales of the forcings in these sensitivity experiments are varied from half to 3 times that in the control (CNTL) experiment (sections 3.1–3.3). The experiments are named following the scales of the forcing as summarized in Table I. The naming convention indicates the change of a multiplication factor in the scales relative to CNTL. For example, H1v1 is the same as CNTL, while H2v0.5 (for example) indicates a doubled horizontal scale and a halved vertical scale.

Figures 6 and 7 show the simulated wave response to different forcings listed in Table I at 210 h. There is much stronger variation of wave structure in the horizontal cross-section (Figure 6) than in the vertical (Figure 7) among the experiments with different forcing scales. In the case that the forcing has small horizontal and vertical scales (e.g. H0.5v0.5 in Figures 6(a) and 7(a), H1v0.5 in Figures 6(d) and 7(d)), the wave packets extend to both cyclonic and anticyclonic regions. If either the horizontal scale or vertical depth of the

Table I. Horizontal and vertical scales R_H and R_z (km) for the nine experiments.

H0.5v0.5	H0.5v1	H0.5v3
(112.5, 0.75)	(112.5, 1.5)	(112.5, 4.5)
H1v0.5	H1v1 (CNTL)	H1v3
(225, 0.75)	(225, 1.5)	(225, 4.5)
H2v0.5	H2v1	H2v3
(450, 0.75)	(450, 1.5)	(450, 4.5)

forcing is increased, more of the wave response appears in the anticyclonic region (e.g. H1v0.5 in Figures 6(b) and 7(b), H2v0.5 in Figures 6(h) and 7(h)). This asymmetry is due to the shear terms and the terms involving u and v perturbations in Eqs (1.1)–(1.5), as discussed in the previous section.

The amplitude of the wave response is also different among these experiments. Increasing the horizontal scale of the wave forcing at a fixed location appears to lead to an increase in wave amplitude, if the vertical scale of the forcing is sufficiently small (e.g. comparing panels (a), (d) and (g), or (b), (e) and (h), in Figure 6). The amplitude dependence on the horizontal scale is less apparent if the vertical scale of the forcing is too large (Figure 6(c), (f) and (i)). The weaker wave response to forcings with very large vertical scales is probably due to the fact that the forcing may be less effectively projected to the modes that are allowed to propagate in the dipole–jet flow.

In short, despite some dependence on the scales of forcing, neither the amplitude nor the horizontal or vertical wavelength of the waves varies monotonically with

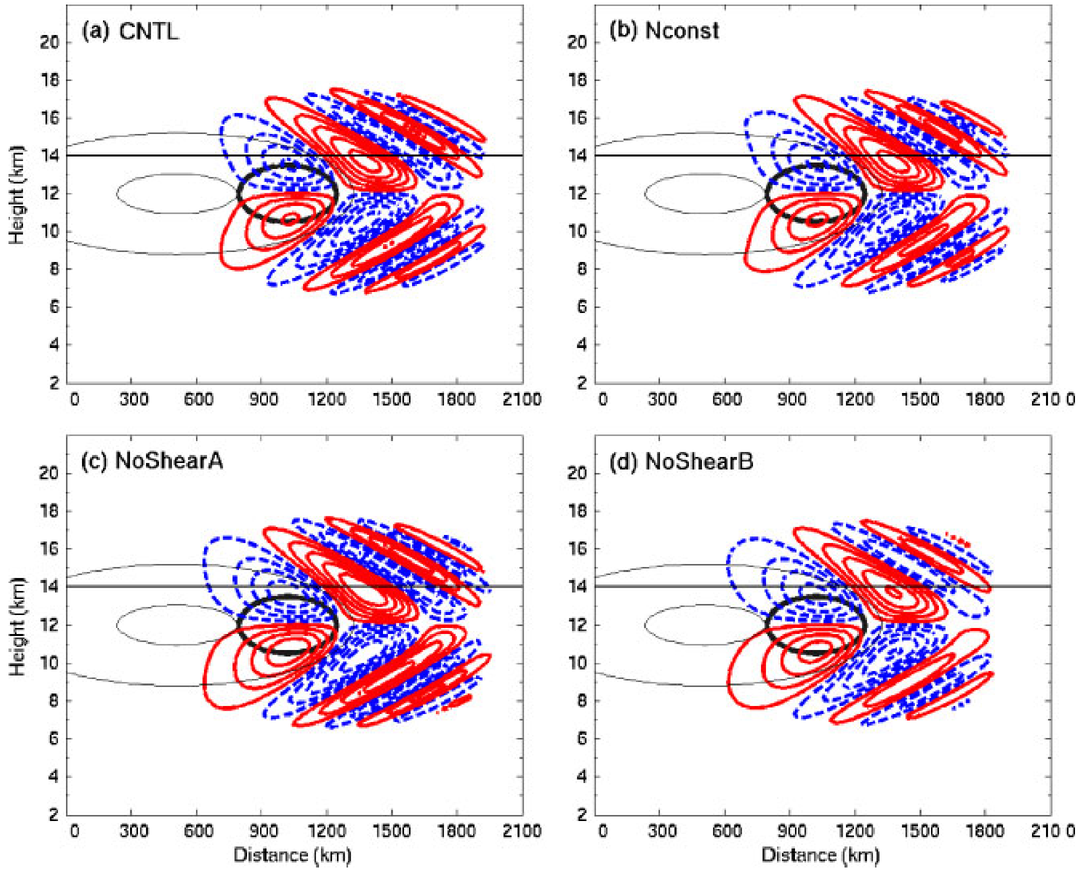

Figure 3. (a) Vertical velocity (ci $= 2.5 \times 10^{-4}$ m s^{-1}, positive, solid; negative, dashed; zero contours omitted) at the cross-section indicated in the corresponding panels in Figure 2 at 210 h from CNTL. (b) Same as (a) except that background static stability is constant (Nconst). (c) As (a) but without the shear terms excluded (NoshearA). (d) As (a) but with all shear terms excluded (NoShearB). The light contours are wind speed (20, 30 m s^{-1}) of the background wind. The solid straight lines indicate the corresponding horizontal cross-sections in Figure 2. This figure is available in colour online at wileyonlinelibrary.com/journal/qj

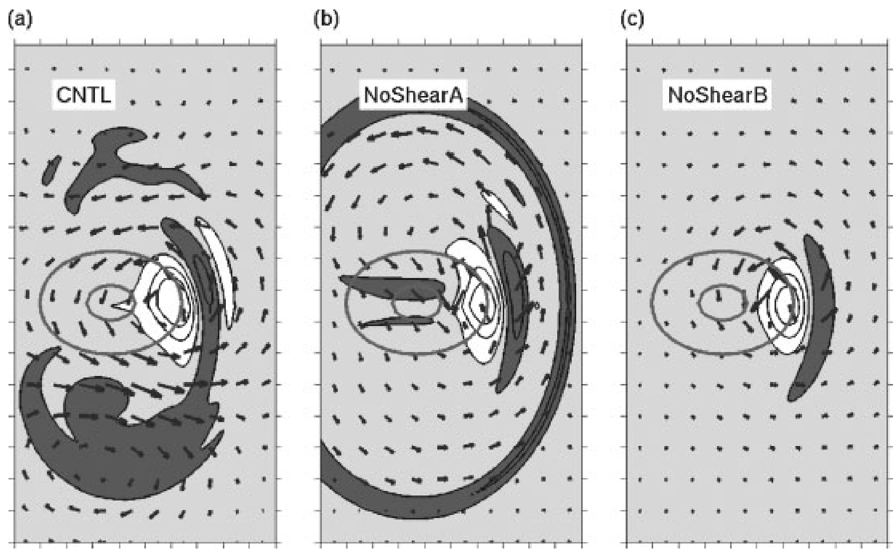

Figure 4. Vertical relative vorticity (every 0.2f, negative shaded, zero omitted), perturbation wind vectors (every 10 grid points) at 210 h, and horizontal wind U_B (20, 30 m s^{-1}) plotted for (a) CNTL; (b) NoShearA; (c) NoShearB. The distance between ticks is 300 km.

the horizontal scale or the vertical scale of the forcing. These results suggest that the background flow (the wave propagation media), besides the scale of the prescribed forcing, is important in determining the spatial structure and amplitude of the wave response. Nevertheless, as the scale of the forcing is increased to the extent that it becomes comparable to the localized jet, balanced and unbalanced flow components become increasingly inseparable. Hence, the results at such a limit must be viewed with some caution.

Figure 7 shows good agreement in the regions of dominant wave activities (corridors of wave packets) and the aspect ratio of the waves (defined as horizontal wave number k over vertical wave number m, or k/m) among these experiments as seen in the vertical plane along the dipole axis. This

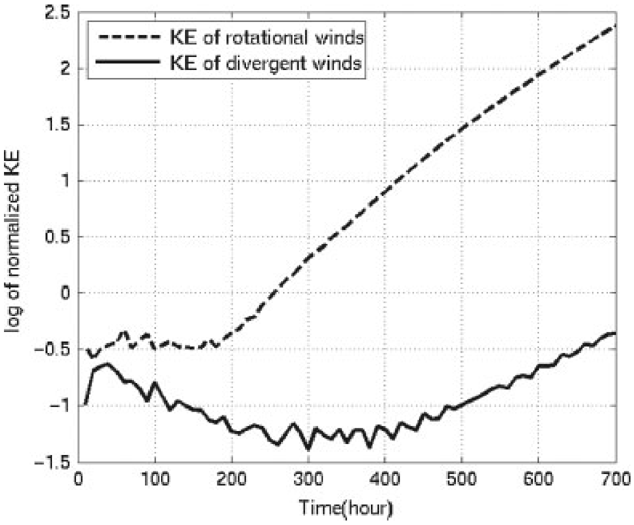

Figure 5. Time series of the logarithm of kinetic energy (KE) associated with rotational winds (dashed) and divergent winds (solid) for CNTL. KE is normalized by the initial total KE.

indicates that the effect of propagation dominates over the source. This is consistent with the wave capture theory that wave packets may be captured in the presence of significant horizontal and vertical wind shear. The importance of a wave capture mechanism in sheared flows has been previously examined in Badulin and Shrira (1993), Bühler and McIntyre (2005), Plougonven and Snyder (2005) and Wang *et al.* (2009).

Bühler and McIntyre (2005) predict that, for captured waves, the wave aspect ratio k/m approaches f/N, the large-scale environmental aspect ratio (0.007 in the current setting). Since the QG dipole flow scales as $Ux/Uz \sim f/N$, where Ux/Uz is the shear aspect ratio, we expect $Ux/Uz \sim k/m \sim f/N$ in the long-time limit of a perfect wave capture. Moreover, since k and m are also related through the dispersion relationship:

$$\omega_i^2 = (Uk)^2 = f^2 + N^2 \cdot \frac{k^2}{m^2}, \tag{6}$$

where the intrinsic frequency $\omega_i = -Uk$ because wave frequency is zero here. Equation (6) predicts that as the mean flow U decreases with height, the horizontal wavelength (wave number) becomes smaller (larger) with respect to height in the stationary background wind, assuming k/m is set according to $Ux/Uz \sim k/m \sim f/N$. Indeed, from lines of constant phase (not shown), we estimate that k/m is approximately 0.007, consistent with the shear aspect ratio $Ux/Uz \sim 0.007$.

Figure 7 also illustrates that the region of constant shear aspect ratio $Ux/Uz \sim 0.007$ collocates with the dominant wave packet in most cases, although the phase tilt of the wave response differs slightly from experiment to experiment with different forcing scales. The mechanism by which wave packets tend to converge to the region of near-constant shear aspect ratio will be further explored through ray tracing analysis in section 4. Figure 7 also appears to suggest that the particular region where Ux/Uz is close to f/N could be used conveniently as an index to predict where wave capture would happen. However, it should be noted that it provides a necessary but not a sufficient condition for wave capture, since other factors may also play a role, e.g. the amount of time that the waves propagate through this region needs to be sufficiently long for the waves to be captured (Snyder *et al.*, 2007; Wang *et al.*, 2009).

In summary, there is good agreement in terms of their wave aspect ratio, wavelengths and regions of pronounced wave packets among these different linear simulations, while horizontal structures and wave amplitudes may vary significantly from experiment to experiment. The wave capture is capable of predicting the wave aspect ratio and wavelengths of the dominant wave response but appears insufficient to explain the location of the waves, which will be explored using ray tracing in section 4.

3.5. *Wave response with different constant background winds*

In previous subsections, the reference flow has a constant wind of $U = -5$ m s^{-1}. Here we vary the reference flow by changing $U = -10$, 0 and 5 m s^{-1} but keep the QG dipole the same. Different reference flow does not alter the balanced nature of the dipole, but will introduce the Doppler shifting effect on the linear gravity waves. The simulated horizontal/vertical wavelengths will be compared with Eq. (6).

Figure 8 displays the wave response at 210 h when the different reference flow, $U = -10$, 0 and 5 m s^{-1}, is added to the dipole in contrast to $U = -5$ m s^{-1} in CNTL. The stationary divergence forcing has the horizontal (vertical) scale of 225 (1.5) km, the same as in CNTL. The horizontal wavelengths near the sources increase as the background wind increases. To estimate the wave horizontal wavelength and mean wind, the distance between the 1st and the 2nd peak of w (Figure 8(a), (c) and (e)) is measured, and the mean wind is taken as the average between two peaks. The estimated horizontal wavelengths are 360, 420, 510 and 630 km, while the mean wind speeds are 10, 12, 15 and 17 m s^{-1}, when the constant reference winds are $U = -10$, -5, 0 and 5 m s^{-1} respectively. The horizontal wavelength indeed increases when the constant background wind increases. On the other hand, the estimated Doppler-shifted frequencies $-Uk$ are $1.70f$, $1.75f$, $1.85f$ and $1.70f$. These values are slighter larger than the frequency in the wave capture limit ($1.4f$). Nevertheless, the background wind shear constrains the wave frequency into the wave capture limit, so the wavelength dependence on the background wind can be explained by Eq. (6). Figure 8 also shows that wave response is not necessarily to be retained in the jet region when U in increased from -10 m s^{-1} to 0 m s^{-1}. This is mostly due to the fact that the critical level of the wave packets is raised to a higher altitude with an increased background wind speed. Furthermore, if the constant reference wind U increased further to 5 m s^{-1} the critical level is nearly absent within the model domain and the wave packet will propagate far away from the jet core, as shown in Figure 8(f).

4. Ray tracing analysis

Here we use ray tracing analysis to understand (1) the symmetry of the wave pattern in both cyclonic and anticyclonic sides of the jet where no shear terms are included in the linear model, and (2) the convergence of the wave energy near the region $Ux/Uz = 0.007$.

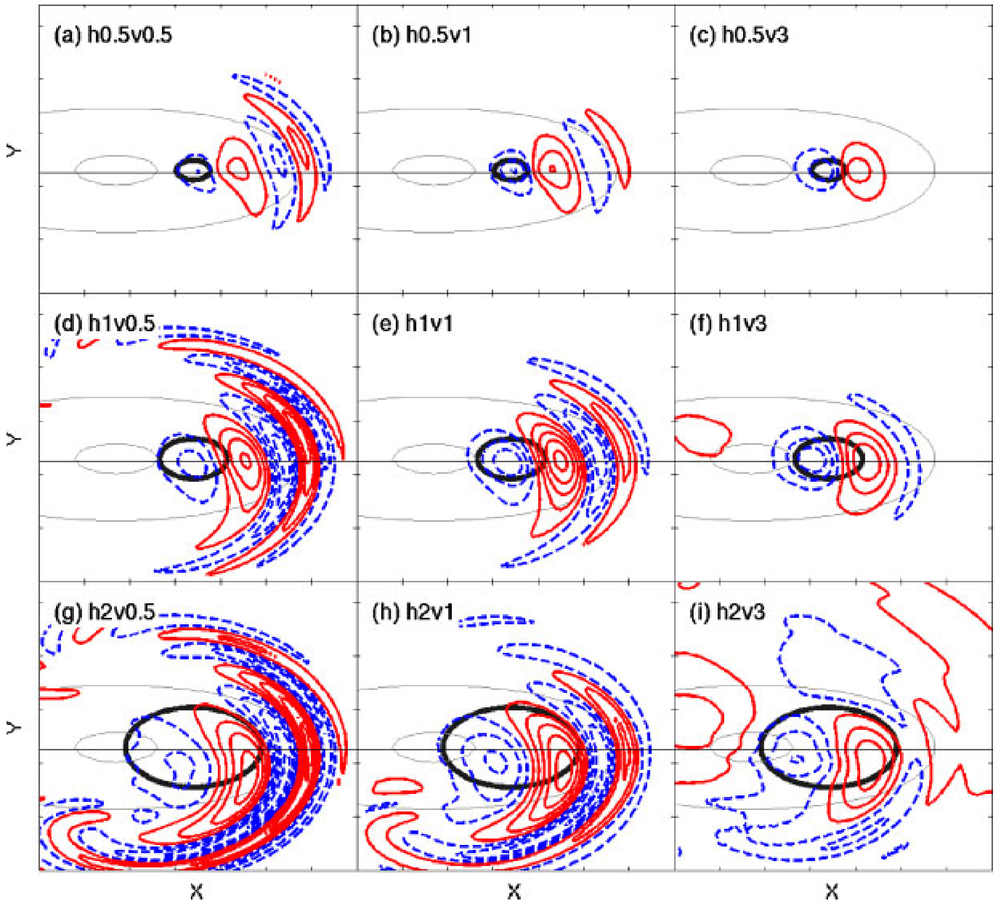

Figure 6. Vertical velocity (ci = 2.5×10^{-4} m s^{-1}, except 1×10^{-4} m s^{-1} in the right panels (c), (f) and (i); positive, solid; negative, dashed) at 14 km due to forcing at different horizontal and vertical scales. A single contour of the forcing term F_δ (1/e of its maximum) is indicated by dark solid lines. Wind in the x direction at 12 km is indicated by solid thin contours (20, 30 m s^{-1}). The solid straight lines indicate the corresponding cross-sections in Figure 7. The distance between adjacent ticks is 300 km. This figure is available in colour online at wileyonlinelibrary.com/journal/qj

4.1. Rays travelling to the cyclonic and anticyclonic region

Three rays are released near the level (1 km below) that the wave pattern is shown in Figure 6 (i.e. 13 km above the ground where the rays are located not too close to the wave sources): one located along the dipole axis, the other displaced symmetrically about the dipole axis, as indicated by the open circles in Figure 9(a). These rays are initialized with horizontal wavelength 700 km, 0 m s^{-1} ground-based phase speed, and wave vectors pointing due west. Other initial wave parameters are derived using the local dispersion relation. These three rays are used to examine ray propagation into the cyclonic and anticyclonic sides of the dipole jet. As shown in Figure 9(a), these rays travel to different regions: one to the north ('N'), one to the south ('S') of their initial locations, and another remains along the dipole axis where it is initiated ('M').

Figure 9(a) shows the projection of these three rays onto the horizontal planes. Ray M travels eastward and upward with the horizontal (vertical) wavelength decreasing gradually to approximately 100 (1.00) km (Figure 9(b)–(c)). Its intrinsic vertical group velocity and horizontal phase speed decrease to near zero at the end of the ray path (Figure 9(d)–(f)). These changes of wave parameters are similar to those in Wang *et al.* (2009), and consistent with the wave capture mechanism.

Rays N and S are initially located symmetrically about the dipole axis. Despite the symmetry in the initial location and background wind with respect the dipole axis, the initial parameters (e.g. vertical wavelength) are slightly different (e.g. Figure 9(b)) due to the asymmetry in static stability (Figure 1). However, the subsequent paths of N and S remain approximately symmetric about the dipole axis. This appears to be consistent with the linear model solution with all the shear wind terms excluded (Figure 2(e)–(f)), which is consistent with the basic assumption of the WKB approximation in the ray-tracing model (Marks and Eckermann, 1995). Thus wave asymmetry, as expected, can not be explained by a WKB approximation-based ray tracing model based on the dispersion relationship for plane waves that excludes the background shear.

Figure 9(d) shows that the x-component wave number k changes sign along the path. This is because the waves follow the background flow (because the group velocity approaches zero) and are thus wrapped around the dipole, hence a change of the wave orientation.

4.2. Rays along the dipole axis plane

Here we release rays from the centre of the forcing (12 km) in the leading edge of the dipole. We use these rays to study the focusing of wave energy into region of $Ux/Uz \sim 0.007$, as revealed in the previous section. The initial horizontal wavelengths of the rays are from 300 km to 1500 km. The initial y component of the horizontal wave number and initial frequency are set to zero. The ray paths remain in the

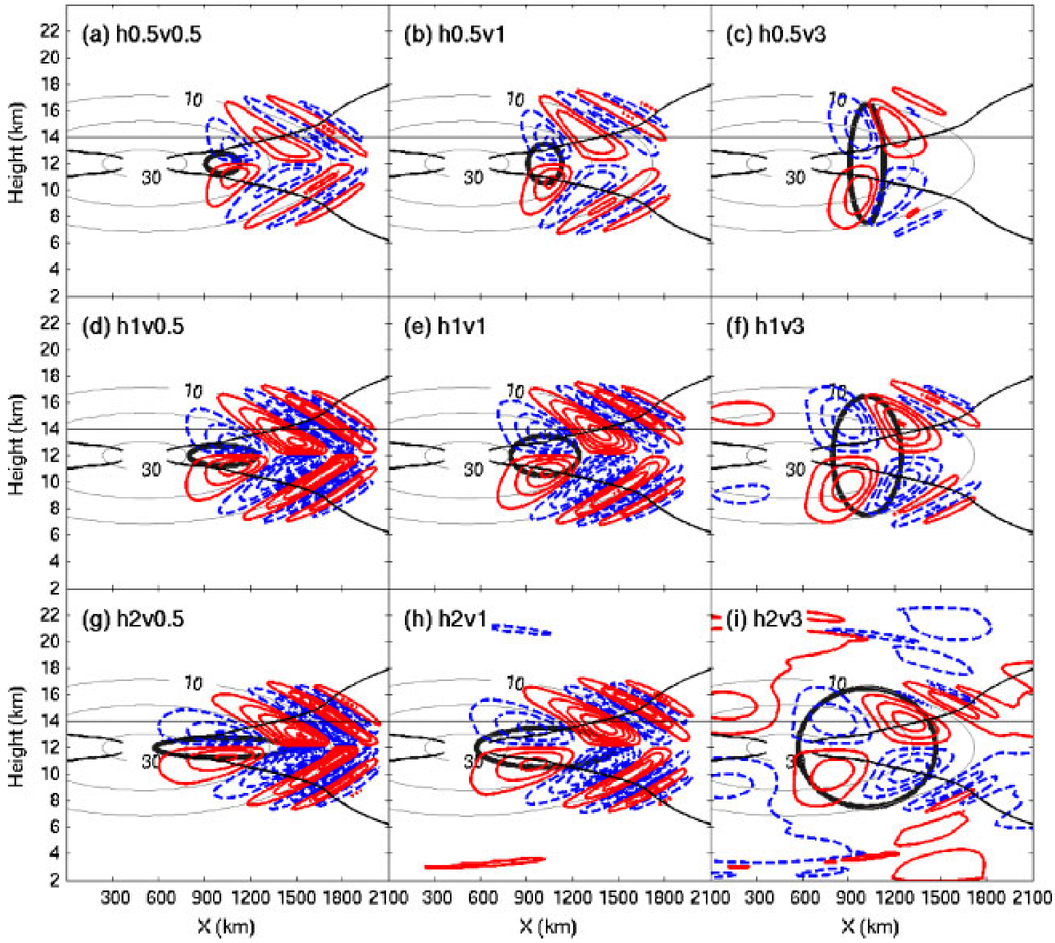

Figure 7. Vertical velocity (ci $= 2.5 \times 10^{-4}$ m s^{-1}, except 1×10^{-4} m s^{-1} in the right panels (c), (f) and (i); positive, solid; negative, dashed) simulated by the linear model due to forcing at different horizontal and vertical scales along the vertical cross-section as indicated by the dark solid line in the corresponding panel in Figure 6. The solid straight lines indicate the corresponding horizontal cross-sections in Figure 6. Wind in the x direction is contoured at (20, 30) m s^{-1}. The thin dark curves in each panel indicate where *Ux*/*Uz* is ±0.007. This figure is available in colour online at wileyonlinelibrary.com/journal/qj

dipole axis plane and do not propagate to either the cyclonic or anticyclonic side.

Figure 10(a) shows the ray paths along the dipole axis overlapped on the wave response simulated in CNTL (Figures 6(e) and 7(e)). There is a tendency for these rays to be focused near the region where the background shear aspect ratio is between 0.005 and 0.009, although no clear convergence of rays is found. The ray focusing area is also consistent with the region of dominant wave response simulated by the linear model. The curved ray paths are different from rays in a constant wind, where the ray paths remain straight lines and all the wave characteristics remain constant. Figure 10(b) illustrates the spatial distribution of the horizontal wavelength λ_H along the x–z plane. At the fixed location in the horizontal direction, λ_H is smaller at high levels than at the lower levels, which is also consistent with the previous analysis from using Eq. (6).

The tendency of wave focusing is closely related to wind shear. Figure 10 shows the shear aspect ratio *Ux*/*Uz* of the dipole flow in curved lines. *Ux*/*Uz* is smaller in the region above the jet core but larger downstream of the jet core. On the other hand, *Ux* and *Uz* have a strong influence on horizontal and vertical wavelengths, as the change of (k, m) along the ray path is proportional to the shear: $D_g k \sim -kU_x$, $D_g m \sim -kU_z$, where $D_g = \partial/\partial t + \mathbf{C}_g \cdot \nabla$ and $\mathbf{C}_g$ is the group velocity. Hence, in the region of large *Ux*, k is affected strongly; in the region of large *Uz*, m is affected strongly. Change of k and m affects group velocity, which determines the ray paths, hence leading to wave focusing. This is discussed below in detail.

Figure 10(a) shows that the rays with initial horizontal wavelength ∼1200 km seem to have a nearly straight path and remain quite close to the contour with $Ux/Uz \sim 0.007$. Other rays will either ‘bend upward’ (to the left) or ‘bend downward’ (to the right) of the initial ray path direction. The rays with initial horizontal wavelengths larger than 1200 km tend to propagate horizontally downstream of the jet core. However, because of the horizontal shear *Ux*, their horizontal wave numbers increase rapidly. Hence their horizontal propagation (Figure 10(c)) slows down, while their vertical group speeds (Figure 10(d)) are not significantly affected by the shear. In consequence, these rays tend to bend upward and to the left of the original ray path direction towards the region of wave capture.

The rays with initial horizontal wavelengths less than 1200 km tend to propagate vertically above the jet core in the region close to their source. However, because of the vertical shear, *Uz*, their vertical wave numbers increase rapidly (not shown). Hence their vertical propagation slows down (Figure 10(c)), while their vertical group speeds are not significantly affected (Figure 10(d)) by the shear. In consequence, these rays tend to bend downward and to the

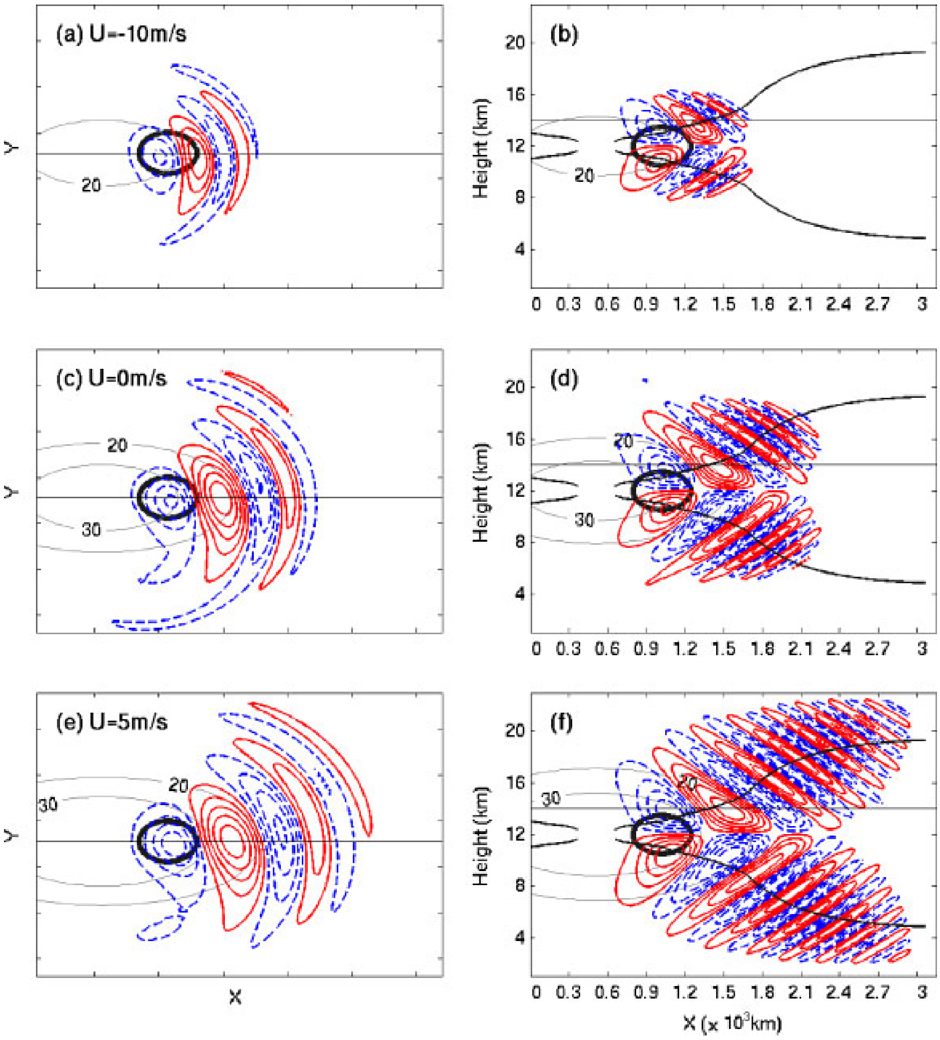

Figure 8. Vertical velocity (ci $= 2.5 \times 10^{-4}$ m s^{-1}, positive, solid; negative dashed) due to the prescribed forcing in the different constant reference flow $U = (-10,\ 0,\ 5)$ m s^{-1} at 14 km in panels (a), (c) and (e), and along the vertical cross-section in panels (b), (d) and (f). The thin dark curves in the right panels indicate where the shear aspect ratio $Ux/Uz = \pm 0.007$. Wind in the x direction is contoured at (20, 30) m s^{-1}. The distance between adjacent ticks in left panels is 500 km. This figure is available in colour online at wileyonlinelibrary.com/journal/qj

right of the original ray path direction towards the region of wave capture.

Change of wave frequency along the rays is also consistent with the above analysis. Figure 10(e) shows that wave intrinsic frequency may change substantially along ray paths for rays with different horizontal wavelengths.

Figure 10(f) shows the wave aspect ratio k/m along the ray paths. There is a broad region where k/m falls between 0.006 and 0.008, which is very close to the shear aspect ratio (the curved lines) in this region. Therefore, for most waves, although the long-time limit of wave capture has not been reached, the tendency of being captured is strong enough to focus these wave packets into a relatively narrow region. The pattern of the intrinsic frequency in Figure 10(c) is similar to that of the wave aspect ratio k/m in Figure 10(f), as expected from the dispersion relation Eq. (6).

In summary, our ray tracing analysis reveals a tendency for the rays to be focused, as is consistent with the linear model simulations. Our ray analysis also provides qualitative explanation of the focusing of wave energy around the region where $Ux/Uz \sim 0.007$.

5. Wave response to prescribed forcing in surface dipole and ray tracing

Wang *et al.* (2009) pointed out the difference in the wave pattern between the mid-level dipole described above and a surface-trapped dipole. In particular, it was shown that gravity waves in the surface vortex dipole are not consistent with wave capture (also in Snyder *et al.*, 2007). To explain the difference, a surface-based QG dipole background is created by prescribing potential temperature anomaly at the surface (which is similar to that in Wang *et al.* (2009) but using a QG-balanced inversion instead of nonlinearly-balanced PV inversion). The potential temperature perturbation is given by:

$$\theta' = \pm 25 \cdot \left\{\cos^2(r_{10} \cdot \pi/2) - \cos^2(r_{20} \cdot \pi/2)\right\}, \qquad (7)$$

where

$$r_{10} = \begin{cases} r_1, \text{if } r_1 \le 10, \\ r_1 = \sqrt{(x-x_1)^2 + (y-y_1)^2}\Big/ R_0, \end{cases}$$

$$r_{20} = \begin{cases} r_2, \text{if } r_2 \le 10, \\ r_2 = \sqrt{(x-x_2)^2 + (y-y_2)^2}\Big/ R_0, R_0 = 1800\text{ km}, \end{cases}$$

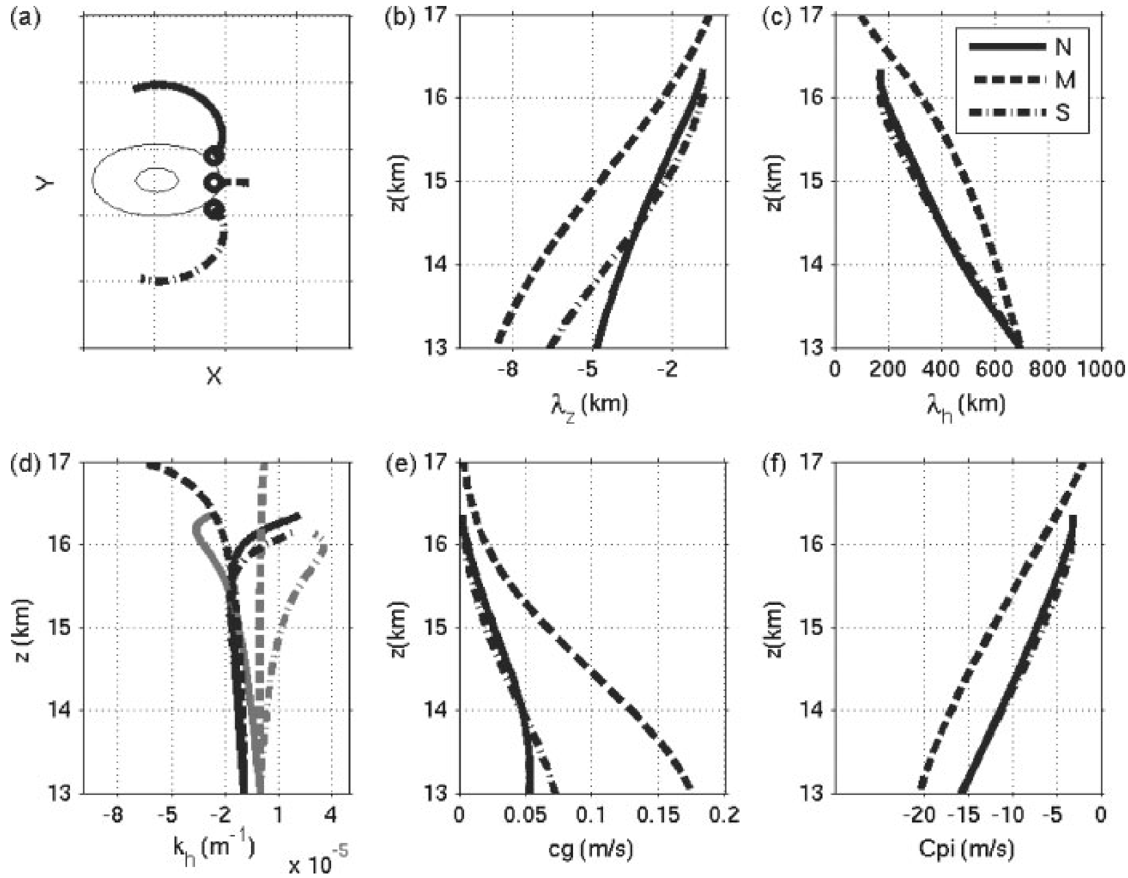

Figure 9. (a) Projection of the three rays, N (solid), M (dashed) and S (dash-dotted), onto the horizontal plane. Zonal wind at 12 km is plotted at (20, 30) m s^{-1} (thin contours). Ray parameters are shown in (b) vertical wavelength, (c) horizontal wavelength, (d) horizontal wave number (x component, dark; y component, grey), (e) vertical group velocity, and (f) intrinsic horizontal phase speed.

with the interior PV set to zero. Besides that, the procedure to produce the surface dipole is very similar to that for the mid-level dipole as introduced in section 2.1. The numerical domain has a dimension of 142 × 211 × 61 grid points in the x, y and z directions and horizontal (vertical) grid spacing of 30 km (200 m). The centre of the vortices is located at $(x1,\ y1) = (54,\ 127.5)$ and $(x2,\ y2) = (54,\ 82.5)$ in grid points, while the forcing is centred at (70, 105). Linear model experiments with prescribed forcings of different horizontal/vertical scales are also performed, in addition to the ray tracing analysis.

Figure 11 shows the wave response and the shear aspect ratio (Ux/Uz) for the surface dipole along the dipole axis, similar to the mid-level dipole simulations in Figure 7. The wave aspect ratio, wavelengths and the dominant region of the wave energy among these different linear simulations agree in different simulations, while the horizontal structure and wave amplitudes vary significantly (not shown) as in Figure 7 of the mid-level dipole simulations. Different from the mid-level dipole simulations, the contour of shear aspect ratio $Ux/Uz = 0.007$ in the surface dipole is located off the jet core, because the dipole is trapped near the surface and vertical wind shear is stronger above the jet core.

Ray calculation is also performed for the surface dipole case. Rays are released from the centre of the forcing (Figure 12) in the surface-level dipole. The initial parameters of the rays are the same as those in the mid-level dipole cases in Figure 10. Similarly, the rays with initially large horizontal wavelength 'bend upward'; the rays with initially small horizontal wavelength 'bend downward'. Corresponding wave parameters vary similarly to those in Figure 10. Nevertheless, the wave focusing seems to be weaker because of different shear structure of the surface dipole wind. Figure 12(a) suggests the rays with initially large horizontal wavelength ($\sim>$900 km) seem to be more focused, while the rays with initially small horizontal wavelength seem to be more dispersive. The region of the shear aspect ratio between 0.005 and 0.009 in the surface dipole is farther away from the forcing than that in the mid-level dipole case. Compared with Figure 10(a), the ray paths in the surface dipole tend to travel a long horizontal distance toward the front of the dipole (Figure 12). Also, there is a difference in the wave aspect ratio k/m between the surface dipole case and the mid-level dipole case. In a broad region of Figure 12(f), k/m is less than or close to 0.005. In contrast, k/m lies between 0.006 and 0.008 in Figure 10(f). Unlike the mid-level dipole, the shear aspect ratio Ux/Uz seems to be larger than k/m along the ray paths in the region where Ux/Uz varies between 0.005 and 0.009. This indicates that the wave capture seems less effective on the waves from the surface dipole because of the difference in the background shear.

In summary, results from linear model simulations and ray analyses of waves in the surface dipole case are mostly consistent with results from the mid-level dipole case. Nevertheless, because the surface dipole has different shear structures, it seems that the wave focusing is less effective for rays with initially short horizontal wavelengths, although wave focusing also occurs.

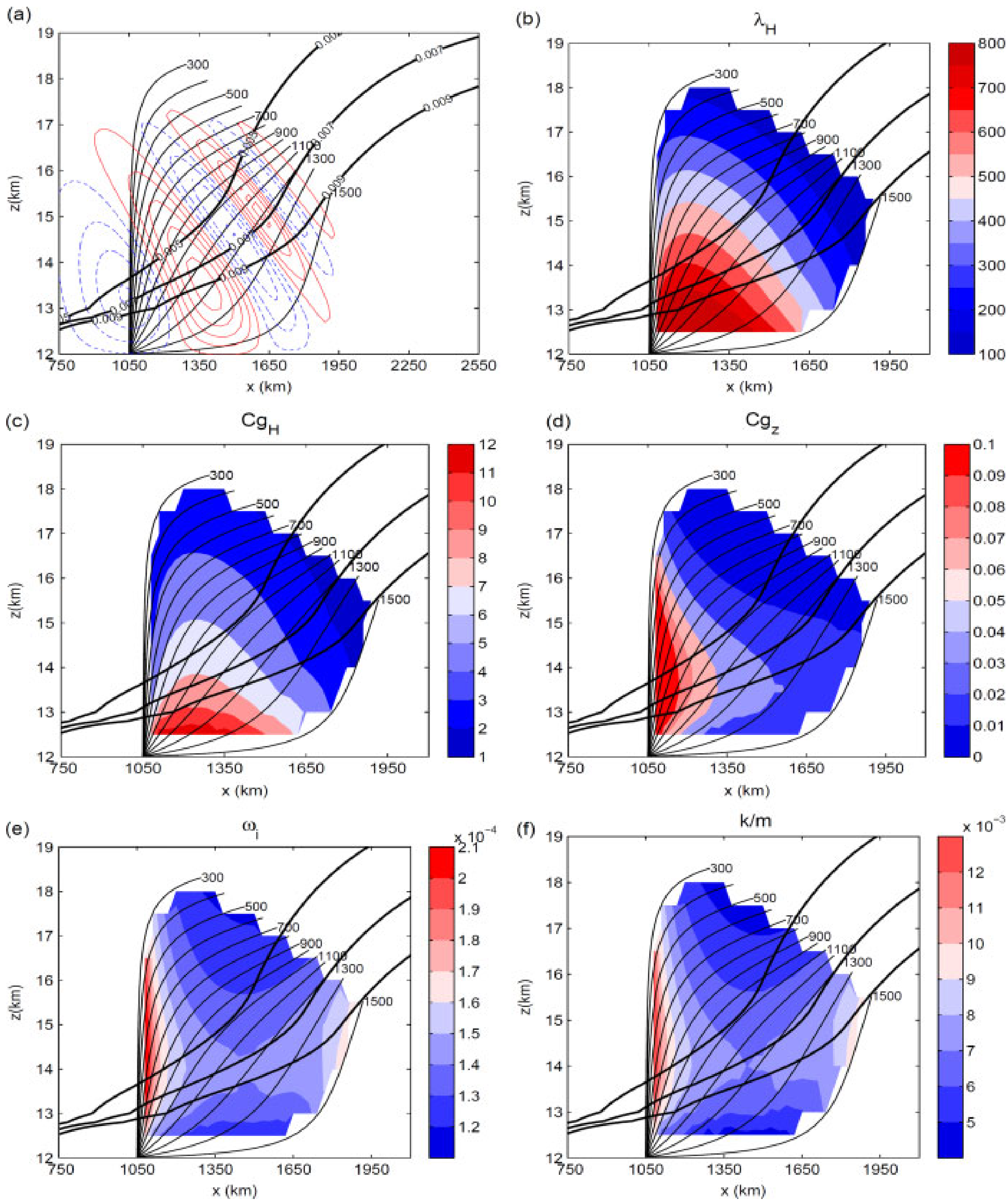

Figure 10. (a) The ray paths of different initial horizontal wavelengths from 300 to 1500 km in a small portion of the domain along the dipole axis in Figure 7(e). Vertical velocity is the same as Figure 7(e). The shaded areas are (b) horizontal wavelength λ_H (km), (c) horizontal group velocity Cg_H (m s^{-1}), (d) vertical group velocity Cg_z (m s^{-1}), (e) intrinsic frequency ω_i (s^{-1}), and (f) the wave aspect ratio (k/m) along the ray paths. The initial wavelength is also labelled for every other ray path in each panel. The curved thick lines in each panel denote the wind shear aspect ratio 0.005, 0.007 and 0.009 from top to bottom. This figure is available in colour online at wileyonlinelibrary.com/journal/qj

6. Summary and conclusions

A linearized compressible, Boussinesq, non-hydrostatic model is developed in this study to examine wave response to prescribed forcing in a kinematically consistent jet flow associated with quasi-geostrophic vortex dipoles. This linear model features horizontal divergence and vorticity as prognostic variables with the inclusion of background shear terms.

It is demonstrated that shear terms can significantly change wave pattern (e.g. wave aspect ratio k/m), and quantitatively change the wave amplitude. The varying static stability in the QG dipole plays a secondary role in the wave response.

Linear model simulations with stationary forcings of different scales are performed to study the dependence of wave parameters on the scale of the forcing. The horizontal structures and wave amplitudes vary significantly, but there is good agreement in terms of their wave aspect ratio, wavelengths and the regions of pronounced wave activities among these linear simulations with forcings of different spatial scales. The wave response (e.g. horizontal wavelengths) away from the source region is largely constrained by the environmental wind shear through the wave capture mechanism. In particular, the

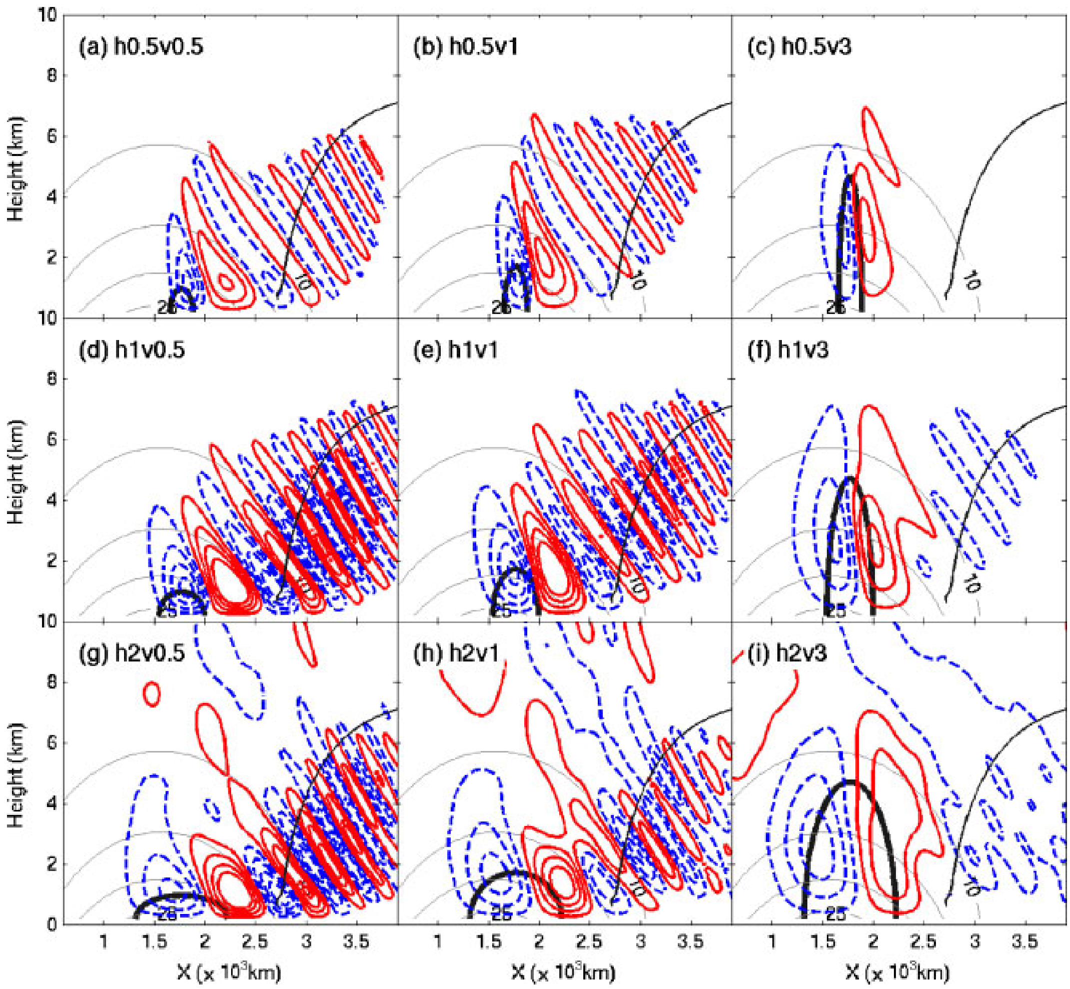

Figure 11. Vertical velocity (ci $= 2 \times 10^{-4}$ m s^{-1}, except 1×10^{-4} m s^{-1} in panels (c), (f) and (i); positive, solid; negative, dashed) due to forcing at different horizontal and vertical scales along the dipole axis from a surface dipole. The single solid thick contour in each panel indicates the forcing F_δ (1/e of its maximum). Wind in the x direction is contoured at (10, 15, 20, 25) m s^{-1}. The thin dark curves in each panel indicate where $Ux/Uz = 0.007$. This figure is available in colour online at wileyonlinelibrary.com/journal/qj

horizontal/vertical wavelengths of the waves are consistent with the wave capture. Further evidence is given by simulating the linear wave response to the Doppler shifting effect, in which case horizontal wavelength is effectively increased. It is also found that the simulated gravity wave activities have the tendency to be focused in the vicinity where the line of constant shear aspect ratio is close to the characteristic large-scale environmental aspect ratio (f/N).

Ray tracing analysis based on the dispersion relation for plane waves does not show significant differences for the wave packet propagating into the cyclonic and anticyclonic regions. This seems to be consistent with the linear model solutions when the shear terms are excluded.

Ray tracing of wave packets along the dipole axis reveals significant change of wave parameters over a range of initial horizontal wavelengths, consistent with the wave capture. On the other hand, ray tracing analysis reveals a tendency for the rays to be focused, as is consistent with the linear model simulations. Our ray analysis also provides a qualitative explanation of the focusing of wave energy around the region of the $Ux/Uz \sim 0.007$. It is demonstrated that the horizontal and vertical shears associated with the jet have different influences upon longer and shorter waves, causing rays to be focused to the vicinity where the line of constant shear aspect ratio is close to the characteristic large-scale environmental aspect ratio (f/N). Therefore, the wave focusing is also a consequence of the wind shear but is not to be explained by the wave capture. It differs from the wave capture in that it is relevant to the ray paths, while the wave capture constrains the wave parameters assuming the shear is known along the ray path.

Similar linear model simulations and ray calculations are also performed for a surface-trapped dipole, and results are mostly consistent with those from the mid-level dipole case. Nevertheless, the surface dipole has different shear structure; the wave focusing is less effective for the rays with short initial horizontal wavelength, although wave focusing also occurs.

The linearized model will be used to examine gravity wave forcing and response in more realistic and complex flows to be reported elsewhere.

Acknowledgements

The authors are thankful to Steve Eckermann for providing the GROGRAT ray-tracing model. The authors are grateful to Chris Snyder and Riwal Plougonven for discussions beneficial to this study, and to three anonymous reviewers for their insightful comments on earlier versions of the manuscript. The research was supported by the NSF Grants ATM-0203238, ATM-0618662 and ATM-0904635.

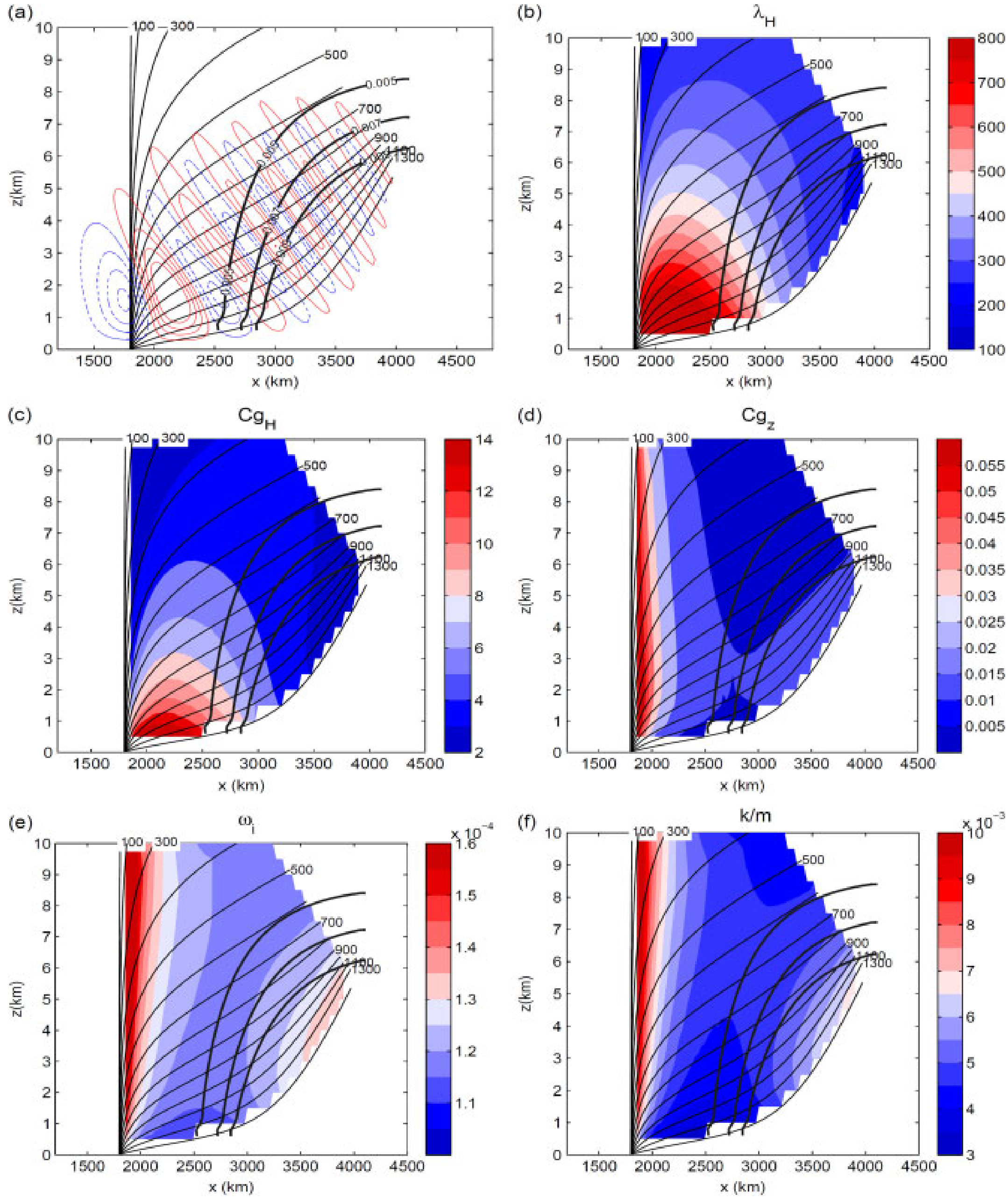

Figure 12. (a) Ray paths of different initial horizontal wavelength from 100 km to 1500 km in a small portion of the domain along the axis of a surface dipole. Vertical velocity is the same as Figure 11(e). (b) Horizontal wavelength λ_H (km), (c) horizontal group velocity Cg_H (m s^{-1}), (d) vertical group velocity Cg_z (m s^{-1}), (e) intrinsic frequency ω_i (s^{-1}), and (f) the wave aspect ratio (k/m) along the ray paths, are shaded. The initial wavelength is also labelled for every other ray path in each panel. The three thick curves in each panel denote the wind shear aspect ratio 0.005, 0.007 and 0.009 from top to bottom. This figure is available in colour online at wileyonlinelibrary.com/journal/qj

References

Badulin SI, Shrira VI. 1993. On the irreversibility of internal-wave dynamics due to wave trapping by mean flow inhomogeneities. Part 1: Local analysis. *J. Fluid Mech.* **251**: 21–53.

Bühler O, McIntyre ME. 2005. Wave capture and wave–vortex duality. *J. Fluid Mech.* **534**: 67–95.

Durran DR. 1999. *Numerical methods for wave equations in geophysical fluid dynamics*. Springer-Verlag: New York.

Epifanio CC, Rotunno R. 2005. The dynamics of orographic wake formation in flows with upstream blocking. *J. Atmos. Sci.* **62**: 3127–3150.

Fritts DC, Alexander MJ. 2003. Gravity wave dynamics and effects in the middle atmosphere. *Rev. Geophys.* **41**: 1003–1063.

Lin Y, Zhang F. 2008. Tracking gravity waves in baroclinic jet-front systems. *J. Atmos. Sci.* **65**: 2402–2415.

Marks CJ, Eckermann SD. 1995. A three-dimensional nonhydrostatic ray-tracing model for gravity waves: Formulation and preliminary results for the middle atmosphere. *J. Atmos. Sci.* **52**: 1959–1984.

O'Sullivan D, Dunkerton TJ. 1995. Generation of inertia–gravity waves in a simulated life cycle of baroclinic instability. *J. Atmos. Sci.* **52**: 3695–3716.

Plougonven R, Snyder C. 2005. Gravity waves excited by jets: Propagation versus generation. *Geophys. Res. Lett.* **32**: L18802, DOI:10.1029/2005GL023730.

Plougonven R, Teitelbaum H. 2003. Comparison of a large-scale inertia–gravity wave as seen in the ECMWF analyses and from radiosondes. *Geophys Res. Lett.* **30**: 1954, DOI:10.1029/2003GL017716.

Plougonven R, Zhang F. 2007. On the forcing of inertia–gravity waves by synoptic-scale flows. *J. Atmos. Sci.* **64**: 1737–1742.

Sato K. 1994. A statistical study of the structure, saturation and sources of inertio-gravity waves in the lower stratosphere observed with the MU radar. *J. Atmos. Terr. Phys.* **56**: 755–774.

Skamarock WC, Klemp JB. 1992. The stability of time-split numerical methods for the hydrostatic and the nonhydrostatic elastic equations. *Mon. Weather Rev.* **120**: 2109–2127.

Skamarock WC, Klemp JB. 1994. Efficiency and accuracy of the Klemp–Wilhelmson time-splitting technique. *Mon. Weather Rev.* **122**: 2623–2630.

Snyder C, Muraki DJ, Plougonven R, Zhang F. 2007. Inertia–gravity waves generated within a dipole vortex. *J. Atmos. Sci.* **64**: 4417–4431.

Snyder C, Plougonven R, Muraki DJ. 2009. Mechanisms for spontaneous gravity wave generation within a dipole vortex. *J. Atmos. Sci.* **66**: 3464–3478.

Swarztrauber P, Sweet R. 1975. '*Efficient FORTRAN subprograms for the solution of elliptic partial differential equations*.' NCAR Technical Note, NCAR-TN/IA-109. Atmospheric Technology Division, National Center for Atmospheric Research: Boulder, Colorado.

Uccellini LW, Koch SE. 1987. The synoptic setting and possible energy sources for mesoscale wave disturbances. *Mon. Weather Rev.* **115**: 721–729.

Viúdez Á. 2007. The origin of the stationary frontal wave packet spontaneously generated in rotating stratified vortex dipoles. *J. Fluid Mech.* **593**: 359–383.

Wang S, Zhang F. 2007. Sensitivity of mesoscale gravity waves to the baroclinicity of jet-front systems. *Mon. Weather Rev.* **135**: 670–688.

Wang S, Zhang F. 2010. Source of gravity waves within a vortex-dipole jet revealed by a linear model. *J. Atmos. Sci.* **67**: 1438–1455.

Wang S, Zhang F, Snyder C. 2009. Generation and propagation of inertia–gravity waves from vortex dipoles and jets. *J. Atmos. Sci.* **66**: 1294–1314.

Wicker LJ, Skamarock WC. 2002. Time-splitting methods for elastic models using forward time schemes. *Mon. Weather Rev.* **130**: 2088–2097.

Wu DL, Zhang F. 2004. A study of mesoscale gravity waves over North Atlantic with satellite observations and a mesoscale model. *J. Geophys. Res.* **109**: D22104, DOI: 10.1029/2004JD005090.

Zhang F. 2004. Generation of mesoscale gravity waves in the upper-tropospheric jet-front systems. *J. Atmos. Sci.* **61**: 440–457.

